Model-based dimensional NDE from few X-ray radiographs: Application to the evaluation of wall thickness in metallic turbine blades

Cédric Fragnaud, Clément Remacha, Julian Andrés Betancur Acevedo, Stéphane Roux

Model-based dimensional NDE from few X-ray radiographs: Application to the evaluation of wall thickness in metallic turbine blades

Cédric FRAGNAUD[1,2], Clément REMACHA[2], Julián BETANCUR[2], and Stéphane ROUX[1]

[1] *Université Paris-Saclay, CentraleSupélec, ENS Paris-Saclay, CNRS, LMPS - Laboratoire de Mécanique Paris-Saclay, 91190, Gif-sur-Yvette, France*
[2] *Safran Tech, 78772 Magny les Hameaux, France*

September 14, 2022

Abstract

The extraction of 3D dimensional measurements based on a *limited* number of 2D X-ray radiographs of a part would offer a significant speed up of quality control procedures in industry. However, there are challenges with respect to both measurements and uncertainties. This work addresses these questions by creating an estimated numerical model of the imaged part, on which dimensional measurements can be made. The numerical model is chosen as a parametric deformation model that encodes the expected variability of the part shape resulting from the manufacturing process. The parameters and uncertainties of the deformation model are estimated by the registration of the computed projections of the model and the observed radiographs. The proposed approach is applied to the NDE of turbine blades manufactured by investment casting, and in particular to the measurement of their wall thickness, which is a critical element. The deformable model consists in partitioning the inner ceramic core into multiple subparts, which may undergo a rigid body motion with respect to the master die. Wall thickness measurements are determined from the estimation of these rigid body motions. To assess the reliability of the proposed procedure, a repeatability study is performed, as well as a direct comparison with ground truth measurements from a reconstructed tomogram. Both of them show that such measurements are reliable and efficient. Furthermore, residual differences between captured and computed projections reveal localized shape deviations from the CAD model, meaning that despite localized model errors, the approach is operable.

Keywords – Shape modeling, Shape parameter estimation, Deformation model, Metrology

1 Introduction

Non Destructive Evaluation (NDE) is performed in industry to control the quality of produced parts ensuring that they meet their technical specifications. The increasing complexity of part geometry calls for developing more advanced NDE methods. The necessity of NDE is even more stringent in sectors where safety is critical, such as aeronautics.

Turbine blades are key parts of aircraft engines. Their complex geometry is meticulously designed and optimized [1, 2, 3, 4] to improve the performance of the engine. In particular, internal air cooling channels allow metal blades to operate at temperatures *higher* than their melting point [5, 6, 7]. These extremely high temperatures are necessary to increase the power and fuel efficiency of aircraft engines. Turbine blades are fabricated following a high precision manufacturing process; nevertheless, geometrical indications — *i.e.* dimensional irregularities of the part that may result in a sub-optimal behavior of the engine — may appear [8]. To ensure the structural integrity of the manufactured turbine blades, it is crucial to have high precision measurements regarding the geometry of the part for quality control.

Coordinate Measuring Machines (CMM) [9, 10] are used to identify external dimensional imperfections. However, they are not suited to detect internal dimensional imperfections (such as cavities or just complex non-convex shapes). To this end, radiographic imaging methods, and in particular X-ray

imaging, have been adopted [11, 12, 13]. The acquisition of a large number of X-ray radiographs allows the 3D image (tomography or tomogram) of the part to be reconstructed. By aligning the nominal model to the reconstructed volume, it is possible to compare the inspected part with its ideal design and extract measurements of deviation. However, this process requires a long acquisition and processing time. Thus, in production lines, each part is observed from a limited number of views. These images are then inspected by specialist operators seeking an unusual gray level difference indicating an irregularity of the part. The measurement of 3D indications from 2D radiographs remains a complex problem for which automated methodology and procedures are highly desirable.

This paper presents a NDE method exploiting a limited number of acquired X-ray images. It relies on the simulation of the X-ray images from a numerical model of the part using an adequate and calibrated projective model [14, 15]. The CAD model is extended to a parametric deformable model so that the projections of the inspected part are registered onto the acquired X-ray images. 3D measurements and the associated uncertainty can be computed on the corrected model, which corresponds to the deformable model computed for the optimal transformation parameters. Section 2 is devoted to describing the developed method. More specifically, a discussion regarding the studied dimensional control, namely the wall thickness measurement, is provided in section 2.1. There, a discussion is proposed on the uncertainty of kinematics based on rigid body motion. The method to identify the optimal transformation parameters is then presented in section 2.2. A deformable model derived from the manufacturing process of turbine blades is proposed in section 2.3. The parameter identification method and the deformable model are the key features that permit the generation of a corrected numerical model. A repeatability study to assess the reliability of the proposed approach to measure the wall thickness of a turbine blade is formalized in section 2.4. It consists of the wall thickness measurement of various samples of a turbine blade, each inspection being repeated multiple times. Section 3 reports and discusses the results of this study. They reveal that, even with the presence of model errors, the method is capable of generating a corrected model comparable to the ground truth (tomogram), which implies similar calculated wall thicknesses.

2 Methods

An NDE procedure to compute variations in the wall thickness of turbine blades based on a limited number of X-ray images has been developed. It requires a deformable model M of the inspected part whose shape is controlled by a set of *transformation parameters*. A registration methodology is proposed to identify the transformation parameters of a reference model of the imaged part that best describe the difference between computed projections and observed radiographs.

Prior to discussing the model parametrization and the method employed to identify the optimal transformation parameters, the principle of the studied dimensional control is introduced.

2.1 Wall thickness metrology

Wall thickness corresponds to the distance between two surfaces $\mathcal{S}_1$ and $\mathcal{S}_2$, be they internal or external. This distance W_{12} is classically defined as

$$W_{12} = \min_{\substack{\boldsymbol{p}_1 \in \mathcal{S}_1 \\ \boldsymbol{p}_2 \in \mathcal{S}_2}} \|\boldsymbol{p}_1 - \boldsymbol{p}_2\|_2 \tag{1}$$

where $\boldsymbol{p}_1$ and $\boldsymbol{p}_2$ correspond to points on surfaces $\mathcal{S}_1$ and $\mathcal{S}_2$, respectively. This definition is however not very convenient from an operational point of view since $\boldsymbol{p}_1$ (resp. $\boldsymbol{p}_2$) has to visit the entire surface $\mathcal{S}_1$ (resp. $\mathcal{S}_2$), and the minimum may not be unique. Hence, in practice, further restrictions can be enforced on $\boldsymbol{p}_1$ or $\boldsymbol{p}_2$. In the following, this distance is computed using the "Ray method" implemented in VG Studio MAX (Volume Graphics GmbH, v 2.2). Namely, an initial point $\boldsymbol{p}_1^0$ is chosen along surface $\mathcal{S}_1$, together with a solid angle of possible search. The closest point to $\boldsymbol{p}_1^0$ along surface $\mathcal{S}_2$ is found, and denoted $\boldsymbol{p}_2^1$. Then, the role of the two surfaces is interchanged, and the closest point to $\boldsymbol{p}_2^1$ along surface $\mathcal{S}_1$ is sought (with the same solid angle restrictions), and its minimum is denoted $\boldsymbol{p}_2^1$. This process is repeated until convergence, where a stationary solution $(\boldsymbol{p}_1, \boldsymbol{p}_2)$ is found. To avoid that the points get out of a neighborhood of the initial point $\boldsymbol{p}_1^0$, it is necessary to consider escape conditions where the process does not converge. In case of success, the resulting distance is noted as $W_{12}(\boldsymbol{p}_1^0)$. This procedure is applied starting for all nodes of the mesh that lie on surface $\mathcal{S}_1$, and finally $W_{12} = \min_{\boldsymbol{p}_1^0} W_{12}(\boldsymbol{p}_1^0)$. Although not

strictly identical to the above mathematical definition, eq. (1), this evaluation of the distance is a very good approximation when a careful choice of neighborhood is made, and hence the exact definition will be considered when required in the theoretical analysis.

In the following, a specific class of transformation applied to the surfaces defining the deformation model will be considered, namely rigid body motions. A brief discussion about their uncertainty is proposed before assessing the fluctuation of wall thickness measurement resulting from a rigid body motion.

2.1.1 Rigid body motion uncertainty

A rigid body motion is mathematically described by the screw theory [16] and can be represented by a rotation $\boldsymbol{R}$ and translation $\boldsymbol{T}(\boldsymbol{q})$ at an arbitrary point $\boldsymbol{q}$. Although $\boldsymbol{R}$ is intrinsic, the translation depends on the chosen reference point $\boldsymbol{q}$. More precisely, if another point $\boldsymbol{q'}$ is chosen, then $\boldsymbol{T}(\boldsymbol{q'}) = \boldsymbol{T}(\boldsymbol{q}) + \boldsymbol{q'q} \times \boldsymbol{R}$.

An aspect that deserves specific comments is the uncertainty of the measured rigid body motion. From image registration, a displacement field can be calculated which can be described by its average $\mathcal{M}_{\boldsymbol{q}} = (\boldsymbol{T}(\boldsymbol{q}), \boldsymbol{R})$ and its fluctuation, $\delta\mathcal{M}_{\boldsymbol{q}} = (\delta\boldsymbol{T}(\boldsymbol{q}), \delta\boldsymbol{R})$. This fluctuation is characterized by a null expectation value and a covariance matrix $\mathbf{C}_{\boldsymbol{q}}$, embedding the rigid body motion uncertainty, composed of three terms, each of which is a 3×3 matrix:

$$\begin{aligned} \mathbf{C}_{\boldsymbol{q}}^{(1)} &\equiv \langle \delta\boldsymbol{T}(\boldsymbol{q}) \otimes \delta\boldsymbol{T}(\boldsymbol{q}) \rangle \\ \mathbf{C}_{\boldsymbol{q}}^{(2)} &\equiv \langle \delta\boldsymbol{T}(\boldsymbol{q}) \otimes \delta\boldsymbol{R} \rangle \\ \mathbf{C}^{(3)} &\equiv \langle \delta\boldsymbol{R} \otimes \delta\boldsymbol{R} \rangle \end{aligned} \tag{2}$$

where $\langle \cdot \rangle$ denotes the average of the quantities within the angle braces, and $\otimes$ the tensor product. The covariance matrix of the rotation, *i.e.* $\mathbf{C}^{(3)}$, is intrinsic. Considering it is a symmetric positive matrix, it can be diagonalized in the basis of eigenvectors $\mathcal{B}$. However, the full covariance matrix $\mathbf{C}_{\boldsymbol{q}}$ is not intrinsic. In particular, the non-diagonal terms of the cross-correlation $\mathbf{C}_{\boldsymbol{q}}^{(2)}$ depend on the chosen reference point $\boldsymbol{q}$. It can be shown that there exists a unique point, denoted $\boldsymbol{q}^*$, such that the antisymmetric part of $\mathbf{C}_{\boldsymbol{q}^*}^{(2)}$ is exactly zero. A privileged frame of reference is then $\boldsymbol{q}^*$ as the origin while the axes orientations are given by $\mathcal{B}$.

2.1.2 Uncertainty of the distance between surfaces

Rigid body motions are applied to the surfaces $\mathcal{S}_1$ and $\mathcal{S}_2$. Because the definition of the distance between surfaces, eq. (1), is not affected by a global rigid body motion affecting both surfaces, only the relative displacement of one surface with respect to the other matters. Thus only $\mathcal{S}_2$ may be considered to be moving while $\mathcal{S}_1$ remains static. The uncertainty of the measurement of W_{12} results from the uncertainty of the rigid body motion affecting $\mathcal{S}_2$. This question is addressed subsequently.

Let $\boldsymbol{p}_1^*$ denote the point on surface $\mathcal{S}_1$ where the minimum distance to $\mathcal{S}_2$ is found, at point $\boldsymbol{p}_2^*$. The surfaces are supposed to be smooth in the neighborhood of $\boldsymbol{p}_1^*$ and $\boldsymbol{p}_2^*$ (no angular edge or corner) so that the surface around them can be described as parabolic. After applying the transformation $\delta\mathcal{M}_{\boldsymbol{q}}$ to $\mathcal{S}_2$, the shortest distance between the surfaces changes. Assuming the rigid body motion $\delta\mathcal{M}_{\boldsymbol{q}}$ is of small amplitude, a first order expansion of the change in distance δW_{12} is found to be a translation along the normal common to both surfaces $\boldsymbol{n} = \boldsymbol{p}_1^*\boldsymbol{p}_2^* / |\boldsymbol{p}_1^*\boldsymbol{p}_2^*|$.

This translation is however not intrinsic as it depends on the point at which the rigid body motion is expressed (section 2.1.1). There exists a unique point $\boldsymbol{q}^*$ for which the antisymmetric part of the cross-correlation between $\delta\boldsymbol{R}$ and $\delta\boldsymbol{T}(\boldsymbol{q}^*)$ in the covariance matrix is null. Thus this point is chosen to compute the statistics of the correlation $\mathbf{C}_{\boldsymbol{q}^*}$, and the orientation of the frame is chosen to be given by the above introduced basis of eigenvectors $\mathcal{B}$. The variance of δW_{12} then reads

$$\left\langle \delta W_{12}^2 \right\rangle = \left(\mathbf{C}_{\boldsymbol{q}^*}^{(1)} + |\boldsymbol{q}^*\boldsymbol{p}_2^*|^2 \, \mathbf{C}^{(3)} \right) : (\boldsymbol{n} \otimes \boldsymbol{n}) + \mathbf{C}_{\boldsymbol{q}^*}^{(2)} : ((\boldsymbol{q}^*\boldsymbol{p}_2^*) \otimes \boldsymbol{n}) \tag{3}$$

where : denotes the double dot product.

These findings rely on the assumption that surfaces are smooth in the neighborhood of $\boldsymbol{p}_1^*$ and $\boldsymbol{p}_2^*$. Additionally, the determination of $\boldsymbol{p}_i^*$ after the transformation $\delta\mathcal{M}_{\boldsymbol{q}}$ requires the curvature tensor $(\boldsymbol{\kappa}_1 + \boldsymbol{\kappa}_2 + W_{12}\,\boldsymbol{\kappa}_1\,\boldsymbol{\kappa}_2)$ to be inverted, where $\boldsymbol{\kappa}_1$ and $\boldsymbol{\kappa}_2$ denotes the curvature tensor of surfaces $\mathcal{S}_1$ and $\mathcal{S}_2$,

respectively. When the two surfaces approach a flat configuration, the inversion give rise to high values, so that the first order approximation assumption must be carefully assessed. The curvature tensor may even become negative, in which case the determination of $\boldsymbol{p}_i^*$ may be unstable. One should note that, even if the position of the points $\boldsymbol{p}_i^*$ becomes variable, the distance W_{12} itself may remain well behaved, but firm conclusions using the above development rest on the assumption that the change in $\boldsymbol{p}_i^*$ remains small.

Therefore, wall thickness should be computed on smooth surfaces and for which the curvature tensor $(\boldsymbol{\kappa}_1+\boldsymbol{\kappa}_2+W_{12}\,\boldsymbol{\kappa}_1\,\boldsymbol{\kappa}_2)$ is well-conditioned (stable inversion) to obtain consistent and reliable measurements. In the following, wall thickness is measured at measurement points located in the airfoil of the blade, in accordance with these recommendations.

2.2 Identification of transformation parameters

Transformation parameters are identified by registering numerically simulated X-ray projections onto the corresponding set of radiographs that constitutes the observations. It is thus essential to consider a simulation tool capable of producing realistic X-ray images accounting for multiple phenomena such as beam hardening and/or scattering, and the appropriate projection geometry [15]. The N acquired radiographs of the inspected part are denoted $P_{\mathrm{a}}^n(\boldsymbol{x}), n \leq N$, where $\boldsymbol{x}$ represents the pixel position and n is the index of the view (different views implying different orientations of the part). Let Π^n be the projection operator for the view n acting on the model M. The acquired images correspond to the projections of a modified version of the model polluted by noise

$$P_{\mathrm{a}}^n(\boldsymbol{x}) \approx \Pi^n[M(\boldsymbol{d})](\boldsymbol{x}) + \eta^n(\boldsymbol{x}) \tag{4}$$

where $\boldsymbol{d}$ is the K-component vector containing the transformation parameters d_k, and $\eta^n(\boldsymbol{x})$ denotes the acquisition noise. Because of the detector and the cone-beam geometry of the source, acquisition noise is not homogeneous and is characterized by a variance that depends on pixel localization, noted as $V^n(\boldsymbol{x})$. Although a dependence on n is not generally expected, the averaging of the images performed during the acquisition of the radiographs is likely to depend on the projection angle to compensate for different attenuations related to the part orientation. The following cost function is introduced

$$\Psi(\boldsymbol{d}) = \sum_n \left\| \frac{1}{\sqrt{V^n(\boldsymbol{x})}} \left(P_{\mathrm{a}}^n(\boldsymbol{x}) - \Pi^n[M(\boldsymbol{d})](\boldsymbol{x})\right) \right\|_2^2 \tag{5}$$

Minimizing this function with respect to $\boldsymbol{d}$ leads to the identification of the optimal transformation parameters. The weight term involving $V^n(\boldsymbol{x})$ accounts for local uncertainties brought by the noise. The weighted L_2-norm in eq (5) is justified as being optimal for the acquisition noise. This problem is solved iteratively using a gradient descent algorithm. At iteration t, the correction vector $\boldsymbol{\delta d}$ corresponds to small perturbations, so that the above cost function is linearized about the solution $\boldsymbol{d}^t = \boldsymbol{d}^{t-1} + \boldsymbol{\delta d}$

$$\Psi_{\mathrm{lin}}(\boldsymbol{\delta d}) = \sum_n \left\| \frac{1}{\sqrt{V^n(\boldsymbol{x})}} \left(P_{\mathrm{a}}^n(\boldsymbol{x}) - \Pi^n\left[M\left(\boldsymbol{d}^{t-1}\right)\right](\boldsymbol{x}) - \Pi^n\left[\boldsymbol{\nabla}_{\boldsymbol{d}} M\left(\boldsymbol{d}^{t-1}\right)\right](\boldsymbol{x}) \cdot \boldsymbol{\delta d}\right) \right\|_2^2 \tag{6}$$

where $\boldsymbol{\nabla}_{\boldsymbol{d}} M$ denotes the derivative of M with respect to $\boldsymbol{d}$. The projection residuals and the sensitivity fields are defined respectively as

$$\rho^n(\boldsymbol{x}) = P_{\mathrm{a}}^n(\boldsymbol{x}) - \Pi^n\left[M\left(\boldsymbol{d}^{t-1}\right)\right](\boldsymbol{x}) \tag{7}$$

$$s_k^n(\boldsymbol{x}) = \Pi^n\left[\frac{\partial M}{\partial d_k}\left(\boldsymbol{d}^{t-1}\right)\right](\boldsymbol{x}) \tag{8}$$

Applying (7) and (8) in (6), the linearized cost function is rewritten as

$$\Psi_{\mathrm{lin}}(\boldsymbol{\delta d}) = \sum_n \left\| \frac{1}{\sqrt{V^n(\boldsymbol{x})}} \left(\rho^n(\boldsymbol{x}) - \sum_k s_k^n(\boldsymbol{x}) \cdot \delta d_k\right) \right\|_2^2 \tag{9}$$

The vector minimizing (6), noted $\boldsymbol{\delta d}^*$, is

$$\boldsymbol{\delta d}^* = \boldsymbol{H}^{-1}\,\boldsymbol{b} \tag{10}$$

where the matrix $\boldsymbol{H} = (H_{ij})$, the Hessian of Ψ_{lin}, and the vector $\boldsymbol{b} = (b_k)$ are given by

$$H_{ij} = \sum_n \sum_{\boldsymbol{x}} \frac{1}{V^n(\boldsymbol{x})}\, s_i^n(\boldsymbol{x})\, s_j^n(\boldsymbol{x}) \tag{11}$$

$$b_k = \sum_n \sum_{\boldsymbol{x}} \frac{1}{V^n(\boldsymbol{x})}\, s_k^n(\boldsymbol{x})\, \rho^n(\boldsymbol{x}) \tag{12}$$

This approach converges towards the minimum of the cost function (5), leading to the identification of the sought vector of transformation parameters $\boldsymbol{d}$. The analysis of the uncertainties in the computed optimal parameters is an indicator of their reliability and is used to assess the quality of the registration. Assuming that the residuals $\rho^n(\boldsymbol{x})$ at convergence mostly contains noise $\eta^n(\boldsymbol{x})$, these uncertainties are extracted from the registration procedure. The uncertainties associated with the estimates δd_i together with their correlations are given by the covariance matrix $\mathrm{C}_{ij} = \langle \delta d_i\ \delta d_j \rangle$

$$\langle \delta d_i\ \delta d_j \rangle = \sum_{k,l} H_{ik}^{-1} H_{lj}^{-1} \sum_{n,m} \sum_{\boldsymbol{x},\boldsymbol{y}} s_k^n(\boldsymbol{x})\, s_l^m(\boldsymbol{y}) \left\langle \frac{\eta^n(\boldsymbol{x})}{V^n(\boldsymbol{x})}\, \frac{\eta^m(\boldsymbol{y})}{V^m(\boldsymbol{y})} \right\rangle \tag{13}$$

The noise is assumed to be Gaussian and white (spatially and temporally uncorrelated) such that

$$\langle \eta^n(\boldsymbol{x})\, \eta^m(\boldsymbol{y}) \rangle = \delta_{nm}\, \delta_{\boldsymbol{x}\boldsymbol{y}}\, V^n(\boldsymbol{x}) \tag{14}$$

where $\delta_{..}$ denotes the Kronecker symbol. Using the previous expression, eq. (13) reads

$$\mathrm{C}_{ij} = \langle \delta d_i\ \delta d_j \rangle = H_{ij}^{-1} \implies \mathbf{C} = \boldsymbol{H}^{-1} \tag{15}$$

The associated correlation matrix $\mathbf{R}$ is defined as

$$\mathrm{R}_{ij} = \frac{\mathrm{C}_{ij}}{\sqrt{\mathrm{C}_{ii}\, \mathrm{C}_{jj}}} \tag{16}$$

2.3 Deformable model of a turbine blade

To best capture the shape of the part, it is necessary to consider a deformable model M describing the expected shape variability. If the chosen deformable model provides a large flexibility, it will involve many degrees of freedom, at the risk of rendering the registration procedure ill-conditionned or even ill-posed. The deformable model thus needs to contain a reasonable number of parameters while describing the desired range of shapes. A deformable model derived from the *a priori* information on the manufacturing process is ideal to mitigate the lack of information due to the limited number of views.

The internal air cooling cavity of a turbine blade describing the internal structure is manufactured by an investment casting process. A ceramic core reproducing the shape of the desired cavity is positioned in the injection mold, known as *master die*. A slight misalignment of the core results in thinner or thicker walls in different regions of the blade compared to its ideal CAD model. Moreover, the core and master die may expand or shrink during the manufacturing process due to thermal constraints, which leads to thickness differences with the blade CAD model. Another potential source of thickness variation is a manufacturing defect in the core or in the master die themselves. However, they are considered negligible as compared to those induced by the core misalignment.

This manufacturing process may be exploited to generate the deformable model. The model M consists in the partition of the part into two main subparts: the master die and the core. The shape of the core is then extracted from the master die (see Figure 1). This model can be enriched depending on the structure or the manufacturing process of the core, for instance by further dividing the core into subparts. In this study, the core has been partitionned into 5 subparts, as illustrated in Figure 1 (middle). Each subpart indexed by k is associated with a transformation denoted τ_k that maps the model of the corresponding subpart into the corrected one. To correctly interpret transformations, they need to be expressed in the same frame of reference, for instance, that of the ideal part CAD model. A corrected model is obtained by applying the transformations τ_k to each subpart.

The kinematics of the subparts that define a simple yet representative deformable model is given by a rigid body motion of the independent subpart k parametrized by $(\boldsymbol{t}_k, \boldsymbol{\alpha}_k)$. $\boldsymbol{t}_k$ denotes the translation

vector of the k^{th} subpart, and $\boldsymbol{\alpha}_k$ its rotation with respect to the center of the bounding box surrounding the initial master die (black point on Figure 1 (right)) which coincides with the origin $\boldsymbol{O}$ of the coordinate system of reference. To account for thermal shrinkage/dilatation of the core, an additional scale factor s affecting all subparts of the core is introduced. This representation assumes that the geometry of each individual subpart perfectly matches its CAD model without deformation of its surface. This parametric deformable model of the turbine blade takes advantage of information about the manufacturing process, and is well suited for NDE. Moreover, the parametric representation of the corrected model allows for a direct interpretation of the origin of possible deviations from the conceived nominal model, and hence it provides insights about the manufacturing process itself and keys for correcting it.

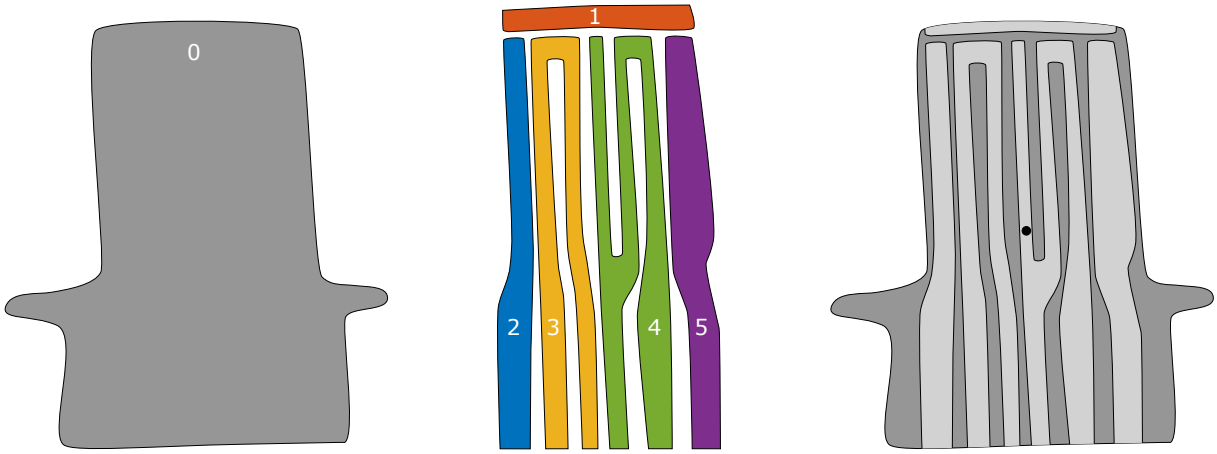

Figure 1: Illustration of the part divided into 6 subparts: the master die (left) and 5 subparts of the core (middle); and their association (right).

The estimation of the parameters s and $(\boldsymbol{t}_k, \boldsymbol{\alpha}_k)$ is achieved following the procedure described in Algorithm 1. The parameters are initialized from the ideal design of the core and of the master die. The convergence criterion is based on the norm of the residuals after each iteration.

Algorithm 1: Iterative registration procedure

Input: Meshes of each subpart, Initial estimates of parameters $\boldsymbol{\mathcal{T}}_c := (s, \boldsymbol{t}_1, \ldots, \boldsymbol{\alpha}_5)$ and $\boldsymbol{\mathcal{T}}_0 := (\boldsymbol{t}_0, \boldsymbol{\alpha}_0)$

Output: Optimal values $\boldsymbol{\mathcal{T}}_c^* = (s^*, \boldsymbol{t}_1^*, \ldots, \boldsymbol{\alpha}_5^*)$ and $\boldsymbol{\mathcal{T}}_0^* = (\boldsymbol{t}_0^*, \boldsymbol{\alpha}_0^*)$

1 Load meshes;
2 **do**
3 **for** $k \leftarrow 0$ **to** 5 **do**
4 Apply the transformation τ_k to the corresponding mesh of the k^{th} subpart;
5 Compute the sensitivity fields for $\boldsymbol{\mathcal{T}}_c$;
6 Compute the sensitivity fields for $\boldsymbol{\mathcal{T}}_0$;
7 Compute $\boldsymbol{\delta\mathcal{T}}_c^*$ using (10) from the sensitivity fields computed at lines 5;
8 Compute $\boldsymbol{\delta\mathcal{T}}_0^*$ using (10) from the sensitivity fields computed at line 6;
9 Update $\boldsymbol{\mathcal{T}}_c \leftarrow \boldsymbol{\mathcal{T}}_c + \boldsymbol{\delta\mathcal{T}}_c^*$ and $\boldsymbol{\mathcal{T}}_0 \leftarrow \boldsymbol{\mathcal{T}}_0 + \boldsymbol{\delta\mathcal{T}}_0^*$;
10 **while** *Convergence criterion reached*;

2.4 Repeatability study

A repeatability study was performed to assess the stability of the method and to evaluate the ability of the deformable model to cope with different parts. Indeed, the acquisition of X-ray images to control a part involves the manual positioning of the sample in the acquisition system which induces human variability. In practice, each control is then realized with a set of (slightly) different viewpoints. Because of their limited number, these viewpoints would contribute greatly to the determination of the transformations τ_k. To eliminate the dependence on the sample positioning in the acquisition system, the transformation

τ_0^{-1} is to be applied to the computed corrected model. The idea behind this is to capture the *relative* motion of the core with respect to the master die, which fully determines the wall thickness. It also allows the computation of wall thicknesses in the same reference frame for all samples. This amounts to only applying the relative transformations $\tau_k^0 := \tau_0^{-1}\tau_k$, $k > 0$ to each subpart of the core. Although it theoretically solves the issue, it is essential for the reliability of the NDE procedure to validate this point.

During the repeatability study, X-ray images of six metallic turbine blades, selected so that they cover or exceed the tolerance interval for the wall thickness measurements, were acquired nine times each. The inspected turbine blades are referred to as samples in the following. The images were acquired with the XT H 450 system developed by Nikon Metrology at the Safran Advanced Turbine Airfoils (PFX) research center; the acquisition parameters are listed in Table 1. During acquisition, the sample was manually positioned in the acquisition system and rotated by intervals of 30°, leading to a total of $N = 12$ projections. The procedure was reproduced for all six samples and all nine repetitions.

For each batch of observed radiographs, the above described parametric deformable model was fitted using Algorithm 1 to generate a corrected model. Wall thickness was measured for 80 points in the airfoil, as mentioned in Section 2.1, using an automatic routine. Surfaces $\mathcal{S}_1$ and $\mathcal{S}_2$ introduced in eq. (1) correspond in practice to sub-surfaces around these measurement points. These sub-surfaces contain between 10 and 30 points each.

For each sample, nine sets of optimal transformation parameters were identified, one for each batch of images. A reasonable assumption of a Gaussian dispersion of the nine batches of transformation parameters allows the uncertainties on the measurements to be computed. This assumption was verified using Shapiro-Wilk normality test [17].

Acceleration voltage	400 kV	Frames per projection	32
Tube current	500 μA	Size of images	2000 × 2000 pixels
Pre-filtering	4 mm of copper	Voxel size	50.55 μm
Exposure time	354 ms	Encoding	16-bit uint

Table 1: Parameters for X-ray image acquisition using a XT H 450 (Nikon Metrology).

3 Results and discussion

Each identified relative transformation τ_k^0 is a combination of a scaling by a factor s, a translation $\boldsymbol{T}_k$ and a rotation specified by Euler angles $\boldsymbol{\theta}_k$. For every sample, the average values of the associated estimates over the 9 sets are presented in Figure 2.

Figure 2 suggests that the transformation parameters show some variability among the different samples. This observation is due to the selection of the parts such that they would represent the production operating range. In this sense, Figure 2 shows the ability of the registration procedure to handle parts that have the same ideal design but whose actual geometry differs due to production variability. In addition, considering that the transformation parameters are noticeable, it confirms to the necessity of taking into account the transformation of the core to perform accurate measurements of wall thicknesses. The large variability of the translation vectors $\boldsymbol{T}_1$ and $\boldsymbol{T}_5$ is due to the choice of the point about which rotations are computed. For rigid body motions, translations are not intrinsic as they depend on the chosen point of rotation (*cf.* subsection 2.1.1). As seen in Figure 1, subpart 1 (red) is far from the center of rotation (black). The curved nature of the blade, not visible in Figure 1, leads to the same conclusion for subpart 5 (purple).

In the following, results will be presented for the sample number 1 as conclusions are similar for all samples. The variability of the identified transformation parameters over the 9 sets is presented in Figure 3. Values have been centered around their median m to better visualize their spread. The figure shows that the variability of the transformation parameters are much smaller than the variability between samples: in the range of 10^{-3} for the scale factor, 35 μm for the translations parameters, and 0.2° for the Euler angles. To properly interpret theses values, the displacements associated with these variabilities need to be computed and compared to the voxel size which is here 50.55 μm. Thus, for each parameter, two transformations are considered: one using the lowest identified value, the other with the highest (the values of the other parameters correspond to their medians). These transformations are applied to the initial model, and the magnitude of the displacement between the two transformed models is computed

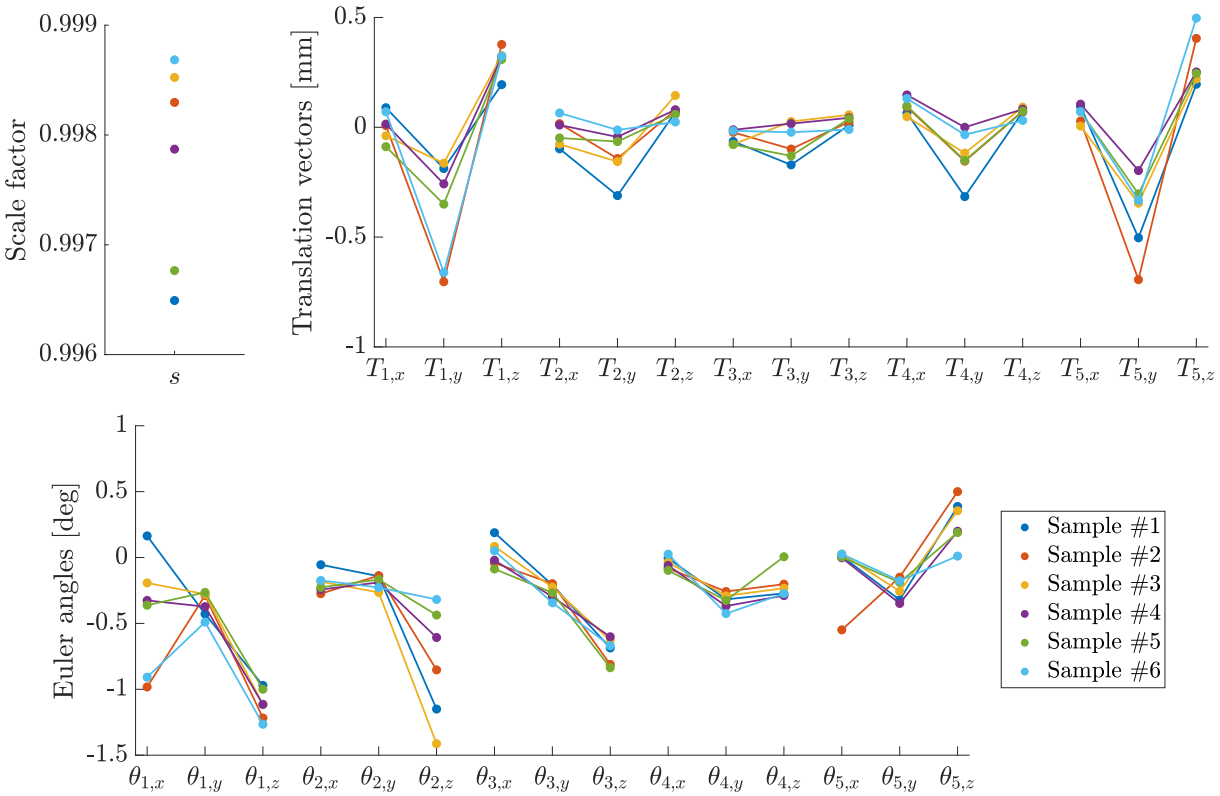

Figure 2: Average values of the transformation parameters for all samples: scale factor s (top left), components of the translation vectors $\boldsymbol{T}_k$ (top right), Euler angles $\boldsymbol{\theta}_k$ (bottom).

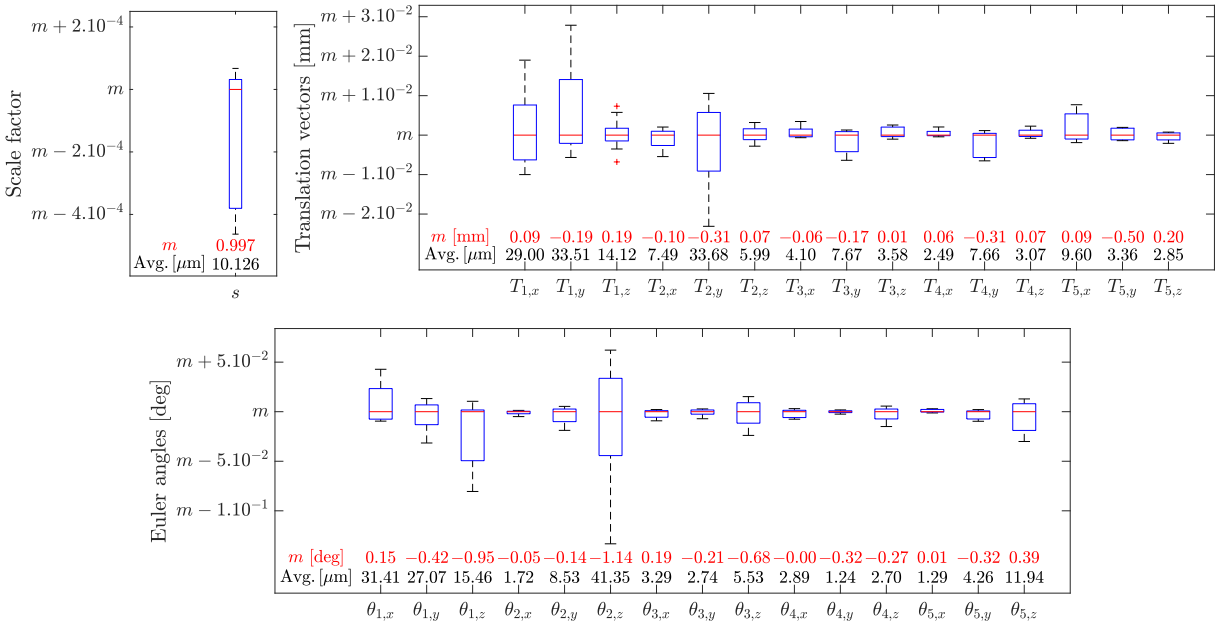

Figure 3: Boxplots showing the variability of the identified optimal transformation parameters over 9 repetitions for sample number 1. Values have been centered around their median m to better visualize their spread. Below each box, the median value (red) and the average magnitude (in μm) of the displacements associated with the observed variabilities (black) are presented.

at each node. For the rotation and translation parameters, this magnitude is averaged over the associated subpart; and for the scale factor, over the entire core. These values, expressed in μm, are reported below each box of Figure 3, in black (second line). A sub-voxel accuracy is observed for all the parameters. The parameter $\theta_{2,z}$, for which the sub-voxel accuracy is barely met, exhibits the largest variability, and thus uncertainty. $\theta_{2,z}$ represents a rotation of the 2$^{\text{nd}}$ subpart, shown in blue in Figure 1, around the Z axis. This can be explained by the cylindrical shape of the subpart with a small radius of gyration and an axis that almost coincides with the Z axis. As a consequence, even a large angle variation induces only a minute displacement along the core boundary.

Using equation (15), the covariance matrices $\mathbf{C}$ are computed. An example of such a matrix is displayed in Figure 4, together with the associated correlation matrix $\mathbf{R}$.

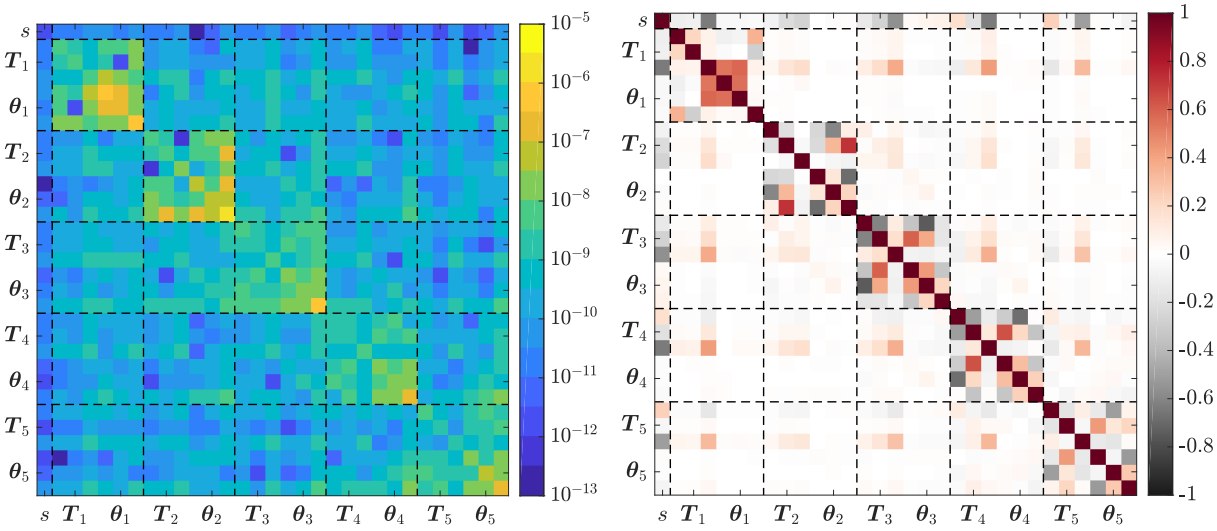

Figure 4: Element-wise absolute value of the covariance matrix $\mathbf{C}$ (left, logarithmic scale) and correlation matrix $\mathbf{R}$ (right) computed at convergence. Black dotted lines are plotted to better visualize the different subparts.

By definition, the diagonal terms of the correlation matrix $\mathbf{R}$ are equal to 1. Non-diagonal terms, which range from -1 to 1, represent the degree of correlation between a pair of parameters. As expected, parameters associated with distinct subparts are weakly correlated (less than 0.5). The scale factor s is mostly (negatively) correlated to the translation parameter along the main orientation of the subpart, as a result of its slenderness.

Figure 5 displays projection residuals with the initial (top) and optimal (bottom) transformation parameters, focusing on four areas of interest. Residual values are expressed as a percentage of the dynamic range of the observed projections. The higher level of residuals in the root of the turbine blade, panel (a), is explained by the fact that some phenomena, particularly visible for high thicknesses, were not included in the projection operator Π^n. It should however be noted that this imperfection in the projection operator is small as it represents at most, in the thickest area, a 5.6% deviation from the gray levels of the observed projections. In the top row, the observed residuals are mainly due to the deviation of the core from its ideal design, as shown for instance in panel (c) where a structure with positive residuals on the left and negative on the right is visible. Similar structures are apparent on the other panels. These deviations may be accounted for by the introduced degrees of freedom. Thus, in the bottom row, the above described structure visible on panel (c) is highly reduced, as well as for the other panels. The procedure leads to the estimates of the best transformation parameters considering the proposed parametrization.

The transformed CAD models are compared to the ground truth given by a tomographic volume, also called tomogram, reconstructed from a set of 3000 radiographs. Figure 6 displays the tomogram (gray) with the initial CAD model (orange) and corrected ones (different shades of blue are used for all 9 estimates). The blue surfaces are barely distinguishable from each other, which confirms the high similarity between the identified sets of transformation parameters. It can be seen that the blue surfaces line up

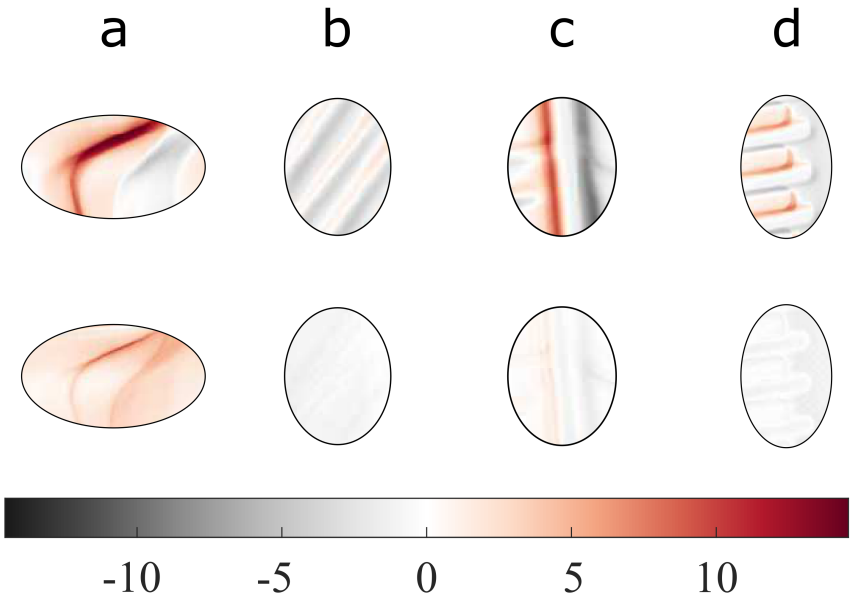

Figure 5: Difference (color) between acquired and simulated projections, before (top) and after (bottom) identification of the transformation parameters. The different panels show: (a) a curved region in the root of the turbine blade, (b) an internal structure, known as a rib structure, in the airfoil, (c) a wall of an internal cavity, (d) slots on the trailing edge of the blade. Values are expressed as a percentage of the observed projections dynamic range.

more tightly with the boundaries of the tomogram than those of the initial CAD model. Discrepancies are observed for the cavity in view (a) or the rib in view (c) which appears shifted. As displayed in Figure 6, these areas are characterized by a high curvature of the surfaces. These incorrect positionings seem to be large, however, the surfaces of these cavities are inclined at a low angle with respect to the section planes. It thus corresponds in 3D to an offset between the surfaces of a very few voxels, namely one or two. Despite the number of radiographs used being reduced by a factor of almost 300, the agreement between the corrected model and the tomogram when the curvature is low is outstanding.

However, some remaining deviations are observed. In view (c), the CAD design displays sharp corners, whereas the ones in the manufactured part are smoother. This discrepancy can be explained by the effect of the sintering of the mold or the surface tension between the metal and the core during the metal casting. As these phenomena are not described in the deformable model, such deviations cannot be resolved.

Thus, even with (hopefully localized) model errors, the proposed deformable model explains most of the differences, which renders the correction efficient and operable. In addition, the observed differences between the part and its CAD model in highly curved regions points towards considering other deviations from the original CAD model, namely non-rigid shape deformations. These deviations may be accounted for by resorting to a more flexible deformable model, for instance, an additional correction model acting at a more local scale. An alternative would be to use a more representative core mesh obtained from actual manufactured cores. Such a procedure would allow to distinguish more clearly between systematic shape deviation due to the manufacturing process and intrinsic variability. In the case where the geometry of the subparts are systematically measured in the control chain, *e.g.* by Non-Contact CMM, this approach would allow one to increase the available *a priori* information without increasing the time allocated for the control. A weighting to the surfaces based on their curvature can also be considered to further reduce the weight of these model errors.

Wall thickness have been measured in the airfoil of the 9 corrected models and of the tomogram. As illustrated in Figure 6, measurements of the transformed models are similar, so that only the average values of the measurements is representative of further data acquisition and processing. Figure 7 (left) shows a Bland-Altman plot [18] to illustrate the disagreement between the two measurement methods. The bias of 26.6 μm indicates the average difference between the two measurement methods. This discrepancy represents slightly more than *half a voxel*, showing the high accuracy of the proposed approach.

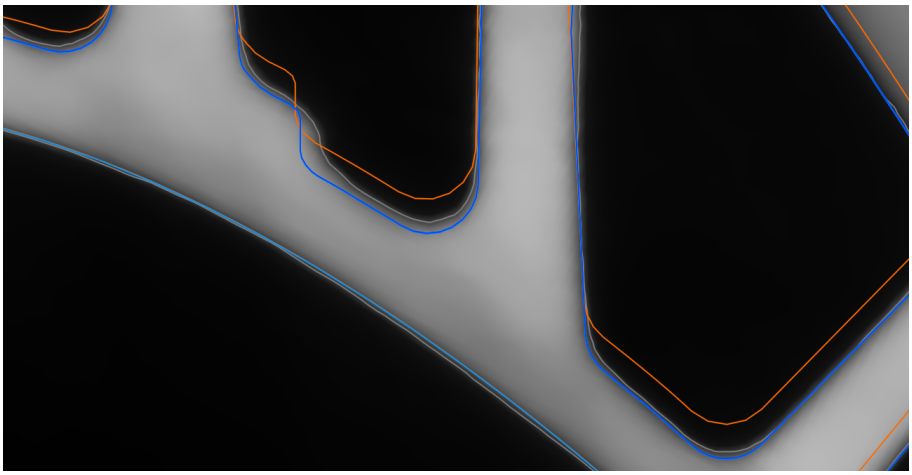

(a)

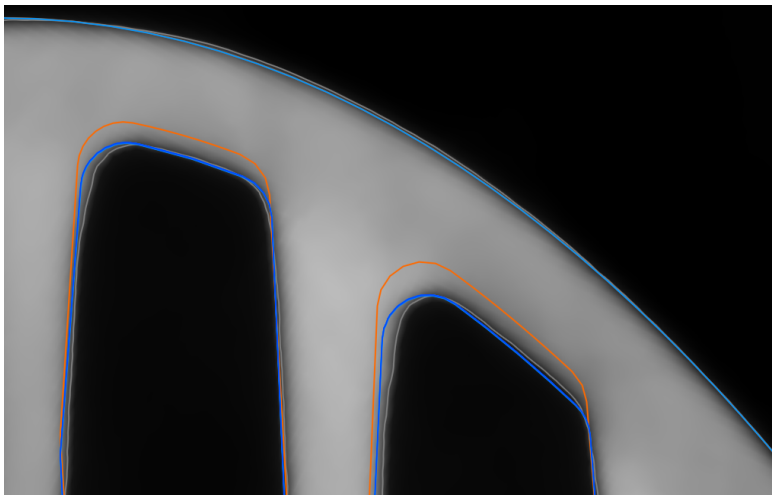

(b)

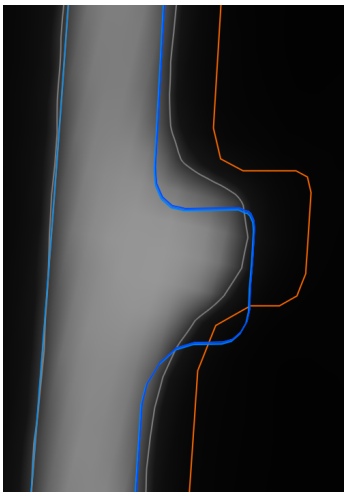

(c)

Figure 6: Superimposition of the ideal (orange) and transformed (shades of blue) designs of the core over the tomogram (gray).

The limits of agreement, which indicate the precision of the measuring system, are to be compared to the tolerance values defined in the part specification. In the case of aeronautical parts for which dimensional compliances are very stringent, this large interval of ≈ 196 μm does not meet the technical requirements. It should however be noted that a less constrained parametrization of the shape would be likely to yield a transformed model closer to reality and thus more accurate measurements. In comparison, the same measurements have been performed on the untransformed model, see Figure 7 right. Using the proposed approach, the bias is increased by a slight amount (15 μm), while the limits of agreement are significantly reduced (185 μm).

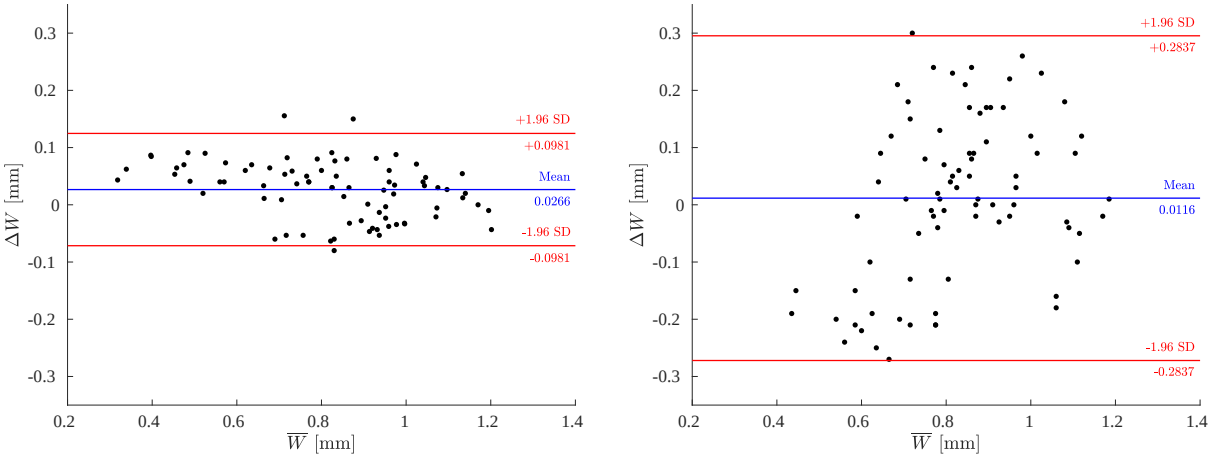

Figure 7: Bland-Altman plot of wall thickness measurements by the proposed model and by X-ray CT tomography. The plot displays the difference ΔW as a function of the mean value $\overline{W}$ of measurements using the corrected (left) and initial (right) models. The mean of the differences (blue line) indicates the bias between the values obtained from the two measurement methods. The limits of agreement (red lines) delineate the interval where 95% of the differences are expected to lie.

The computation of measurement uncertainties based on the covariance matrix $\mathbf{C}$ produced estimates of the order of a few hundred nanometers, which is significantly lower than the uncertainty values obtained by repeating the same control several times. The formula (13) used for the computation of $\mathbf{C}$ relies on the assumption that the residual ρ^n mostly contains noise η^n. For this assumption to be verified, it is necessary to have a transformed model that exactly matches the imaged part and a perfect projection operator. From the previous results, it appears that these two conditions are not met. Figure 6 displays differences in geometry between the estimated model and the ground truth, mainly because the non-rigid deformation of the core is not included in the deformable model. In addition, Figure 5 suggests imperfections in the projection operator which, although small, violate the assumption.

The findings of this study do have some limitations. A limitation of the approach is that the proposed deformable model is presumably too simple to account for the exact shape mismatch. Ideally a flexible model would be required, however, an important feature is the parametrization of the considered deformation modes. The ones considered in this work (independent rigid body motions) benefits from a parametrization that is neither too rich (large uncertainty) nor too poor (realism of shape deviations). It is this trade-off that motivated the decision to define the modes as independent rigid body motions. This trade-off leaves a margin of error which leads to residual shape deviations between the transformed model and the tomogram and thus unreliable measurements. To improve the set of transformations one may envision a more flexible deformable model, adding a local correction model, or replacing CAD models of the surfaces with measured ones. Furthermore, projection residuals (above denoted ρ^n) are indicators of the registration quality and thus of the reliability of the computed measurements. They may also be used to identify the most appropriate locations for the measurement points.

It is worth noticing that the images were acquired in a single X-ray cabin (XT H 450), which may constitute a bias in the analysis. Likewise, the procedure was tested on parts of a single type, *i.e.* a single reference of a turbine blade, even if multiple samples were imaged to account for shape variability. It is however expected that similar results would be observed for a different acquisition system or reference

of a turbine blade with a comparable manufacturing process as no other assumptions other than the manufacturing process have been made. However, accounting for *e.g.* the panel detector used in the X-ray cabin may enrich the projection operator. From an industrial point of view, endorsing the procedure would require that the same study be performed with multiple parts to ensure that a change in the blade geometry would not lead to inconsistent results. Nevertheless, nothing currently suggests that additional issues are to be encountered.

4 Conclusion

In this work, an approach to assess 3D dimensional measurements of complex shape parts from a limited number of 2D X-ray images has been presented. It consists of fitting a parametric model of the imaged part to generate a corrected numerical model. The dimensions to be controlled are measured directly on this corrected model. The selected application case is the control of wall thicknesses of a hollow turbine blade, a part with complex internal geometry. Describing the control principle allowed the definition of guidelines to perform reliable measurements. The optimal transformation parameters of the model are identified by iteratively matching the projections simulated from the transformed model to the observed projections. The parametric model has been developed in line with the manufacturing process. It relies on the partition of the part into multiple subparts: one representing the external surface, five representing the various element of the inner ceramic core describing the internal geometry. The kinematics of each subpart is a rigid-body motion, plus a scale factor to account for thermal constraints experienced by the ceramic core during metal casting. This sparse model mimics what occurs during manufacturing and thus provides a fair description of the expected shape variabilities. In addition, the observed transformations can be further exploited to improve the manufacturing process and reduce the range of shape deviations.

The reliability of the approach was verified *via* a repeatability study where only a slight discrepancy in the identified parameters, and thus in the associated corrected models, was observed. Furthermore, the agreement between measurements computed from the transformed models and reference values computed from a tomogram demonstrated the approach performance. Discrepancies are mostly explained by the non-rigid shape deformations not considered in the simple deformable model proposed here. These discrepancies, although small, do not comply with the very demanding requirements for NDE of turbine blades. Suggestions to mitigate the discrepancy are proposed and include the use of measured surfaces, or the introduction of a more flexible deformable model.

It is worth emphasizing that the proposed methodology has been designed to minimize the acquisition noise error, as expressed in eq. (5). This error is currently much lower than other elements of uncertainty and as a consequence, the method leads to an over-quality. One can consider faster, therefore noisier, acquisitions while still remaining below the uncertainties due to other factors.

Acknowledgement

This work was supported by the French "Association Nationale de la Recherche et de la Technologie" (CIFRE n° 2019/0793). The first and second authors would like to thank Mr. Omer Unlu and Mr. Pierre-Luc Patard for their implication in the experimental phase. The authors would like to thank Ms. Tonya Rose from the Digital Sciences and Technologies Department at Safran Tech for her insightful suggestions on the manuscript.

References

[1] Clemens Buske, Alexander Krumme, Thomas Schmidt, Christian Dresbach, Sascha Zur, and Rdiger Tiefers. Distributed Multidisciplinary Optimization of a Turbine Blade Regarding Performance, Reliability and Castability. In *Turbo Expo: Power for Land, Sea, and Air*, volume 49712. American Society of Mechanical Engineers Digital Collection, 2016.

[2] Mathias Luers, Max Sagebaum, Sebastian Mann, Jan Backhaus, David Grossmann, and Nicolas R. Gauger. Adjoint-based Volumetric Shape Optimization of Turbine Blades. In *2018 Multidisciplinary Analysis and Optimization Conference*. American Institute of Aeronautics and Astronautics, 2018.

[3] Jiaqi Luo and Yao Zheng. Aerodynamic Shape Optimization of a Turbine Blade Considering Geometric Uncertainty Using an Adjoint Method. In *Turbo Expo: Power for Land, Sea, and Air*, volume 58578. American Society of Mechanical Engineers Digital Collection, 2019.

[4] Chun-Yi Zhang, Ze Wang, Cheng-Wei Fei, Zhe-Shan Yuan, Jing-Shan Wei, and Wen-Zhong Tang. Fuzzy Multi-SVR Learning Model for Reliability-Based Design Optimization of Turbine Blades. *Materials*, 12(15):2341, 2019.

[5] S. Dhivya and A. Karthikeyan. Design and Analysis of Gas Turbine Blade with Cooling. *EAI Endorsed Transactions on Energy Web*, 5(20), 2018.

[6] Mohammed Aljibory, Farhan Lafta, and Hasan Qahtan. Review Of Heat Transfer Enhancement In Air-Cooled Turbine Blades. *International Journal of Scientific & Technology Research*, 9:3123–3130, 2020.

[7] Farah Nazifa Nourin and Ryoichi S. Amano. Review of gas turbine internal cooling improvement technology. *Journal of Energy Resources Technology*, 143(8):080801, 2021.

[8] Jonas Aust and Dirk Pons. Taxonomy of Gas Turbine Blade Defects. *Aerospace*, 6(5):58, 2019. Publisher: Multidisciplinary Digital Publishing Institute.

[9] Robert J. Hocken and Paulo H. Pereira. *Coordinate measuring machines and systems*, volume 6. CRC press Boca Raton, FL, 2012.

[10] Grzegorz Budzik. Geometrical accuracy of aircraft engine turbine blades. *Oficyna Wydawnicza Politechniki Rzeszowskiej, Rzeszw*, 2013.

[11] Radosaw Przysowa, Marek Chalimoniuk, Danuta Grzelka-Gajek, Ruslan Shakalo, and Artem Karpenko. CT Inspection of Cooled Turbine Blades. *Journal of KONBiN*, 50(3):307–331, 2020.

[12] Jzef Bachnio, Marek Chalimoniuk, Artur Kuaszka, Henryk Borowczyk, and Dariusz Zasada. Exemplification of detecting gas turbine blade structure defects using the x-ray computed tomography method. *Aerospace*, 8(4):119, 2021.

[13] Scott Hastie, Anthony Chan, Kevin Wiens, Doug Nagy, Robert Tollett, and Paul Lowden. Computed Tomography Wall Thickness Inspection to Support Gas Turbine Blade Life Extension. In *Turbo Expo: Power for Land, Sea, and Air*. American Society of Mechanical Engineers Digital Collection, 2021.

[14] Wim Van Aarle, Willem Jan Palenstijn, Jeroen Cant, Eline Janssens, Folkert Bleichrodt, Andrei Dabravolski, Jan De Beenhouwer, Kees Joost Batenburg, and Jan Sijbers. Fast and flexible X-ray tomography using the ASTRA toolbox. *Optics express*, 24(22):25129–25147, 2016. Publisher: Optical Society of America.

[15] Cédric Fragnaud, Clément Remacha, Julián Betancur, and Stéphane Roux. CAD-based X-ray CT calibration and error compensation. *Measurement Science and Technology*, 33(6):065024, 2022.

[16] Fedor Menas'evich Dimentberg. *The Screw Calculus and Its Applications in Mechanics*. Air Force Systems Command. FTD, Foreign Technology Division. Foreign Technology Division, WP-AFB, 1968.

[17] Samuel Sanford Shapiro and Martin Bradbury Wilk. An analysis of variance test for normality (complete samples). *Biometrika*, 52(3/4):591–611, 1965.

[18] John Martin Bland and Douglas Graham Altman. Statistical methods for assessing agreement between two methods of clinical measurement. *The lancet*, 327(8476):307–310, 1986. Publisher: Elsevier.